JMEPEG (2021) 30:5506–5514
https://doi.org/10.1007/s11665-021-05909-8

©ASM International
1059-9495/$19.00

Corrosion Behavior of a Selective Laser Melted Inconel 718 Alloy in a 3.5 wt.% NaCl Solution

Yanbing Tang, Xinwang Shen, Yanxin Qiao, Lanlan Yang, Jian Chen, Daohua Lu, and Zhongyu Zhang

Submitted: 17 February 2021 / Revised: 27 April 2021 / Accepted: 7 May 2021 / Published online: 26 May 2021

The corrosion behavior of an Inconel 718 alloy fabricated using the selective laser melting (SLM) technique in a 3.5 wt.% NaCl solution is determined. The corrosive effect of the NaCl solution on the Inconel 718 alloy is investigated using potentiodynamic polarization curve measurements, Mott-Schottky plots, electrochemical impedance spectroscopy, atomic force microscopy, and x-ray photoelectron spectroscopy (XPS) and is compared with that on a commercially rolled Inconel 718 alloy (R 718). Electrochemical results suggest that the application of SLM to the Inconel 718 alloy lowers its corrosion resistance. The passive films formed on both alloys show p-type and n-type semiconductor behaviors. However, the concentrations of the defects in the passive films formed on the surface of the SLM Inconel 718 alloy are higher than those on the surface of the commercially rolled R 718. XPS shows that the passive film formed on the SLM Inconel 718 alloy has a higher NiO content, leading to the deterioration of its protective properties.

Keywords additive manufacturing, corrosion, inconel 718, passive film

1. Introduction

Nickel-based superalloys are widely used in the medical biomaterial, aerospace, and national defense fields because of their excellent mechanical properties and superior corrosion resistance (Ref 1-6). As a popular nickel-based superalloy, the Inconel 718 alloy is generally used to fabricate engine turbine disks, turbine rotor blades, and other mechanical fastening parts (Ref 7-9). Usually, these components possess complex structures and cannot be manufactured using normal manufacturing techniques (e.g., wrought, rolling, and casting) (Ref 10). Under these circumstances, additive manufacturing (AM) is adopted to fabricate these components with complex structures.

Although the AM technique has a series of unique features (e.g., shortens the processing steps, can build components with complex shapes, and saves labor costs) and has been successfully applied in practice; however, alloys made using this technique have demonstrated higher corrosion susceptibility than alloys made using traditional manufacturing techniques (Ref 11-14). When exposed to corrosive media, passive films usually form on the surfaces of these alloys, which are found to be defective (Ref 10, 15). Kong et al. (Ref 16) found that the superhigh subgrain boundary density and the microgalvanic effect contributed to the lower passive current density of as-received selective laser-melted 316L stainless steel (SLM 316L SS) without obvious pores. The corrosion performance of AM alloys generally relies on the structures and properties of the passive films that form; thus, it is important to consider the changes in the corrosion properties of AM alloys fabricated using new techniques, e.g., selective laser melting (SLM), wire arc additive manufacturing (WAAM) and laser engineered net shaping (LENS) (Ref 17). Wu et al. (Ref 18) compared the corrosion behavior of a Ti-6Al-4V alloy made using the WAAM technique to that of a wrought alloy; the corrosion resistance of the WAAM-made Ti-6Al-4V alloy in a 3.5 wt.% NaCl solution was lower than that of the wrought alloy due to the change in the passive film thickness. Moreover, the anisotropic microstructure would lead to anisotropic corrosion behavior for the AM parts (Ref 19, 20). Ni et al. (Ref 19) reported that the grain sizes of SLM 316L SS in the XOZ plane were smaller than those in the XOY plane and that the molten pool boundaries would be preferentially corroded. Kong et al. (Ref 20) found that when the aggressive environment was intensified, the existence of voids and molten pool boundaries accelerated the dissolution rate. Juillet et al. (Ref 21) investigated the isothermal oxidation behaviors of casted, forged, and additive manufactured IN-718 superalloys by SLM at 600 °C, 700 °C, and 800 °C and found that the morphologies of the Cr_2O_3 scales depended on the manufacturing process. The oxide scale grown on the AM IN-718 surface appeared more compact than that grown on the forged IN-718 surface. The electrochemical characteristics in the anodically polarized region were similar to those of the traditionally manufactured and AM Ti-6Al-4V alloys. At potentials higher that 2.0 V, the AM samples exhibited a sharp increase in current by over two orders of magnitude due to the microstructural defects and voids (Ref 22). Zhang et al. (Ref 12) found that the corrosion resistance of IN718 fabricated using WAAM was lower than

This invited article is part of a special topical focus in the *Journal of Materials Engineering and Performance* on Additive Manufacturing. The issue was organized by Dr. William Frazier, Pilgrim Consulting, LLC; Mr. Rick Russell, NASA; Dr. Yan Lu, NIST; Dr. Brandon D. Ribic, America Makes; and Caroline Vail, NSWC Carderock.

Yanbing Tang, Daohua Lu, and **Zhongyu Zhang**, Marine Equipment and Technology Institute, Jiangsu University of Science and Technology, Zhenjiang 212003, China; **Xinwang Shen, Yanxin Qiao,** and **Lanlan Yang**, School of Materials Science and Technology, Jiangsu University of Science and Technology, Zhenjiang 212003, China; **Jian Chen**, School of Materials Science and Technology, Jiangsu University of Science and Technology, Zhenjiang 212003, China; and Department of Chemistry and Surface Science Western, Western University, London, ON N6A 5B7, Canada. Contact e-mails: yxqiao@just.edu.cn and lanlanyang@just.edu.cn.

that of wrought alloy, which was due to the presence of a high percentage of porous and less protective NiO in the passive film, which formed on the surface of WAAM IN718. Research on the corrosion behaviors of SLM alloys remains in its infancy (Ref 23, 24). Thus, further research is needed to better elucidate the effect of SLM on the corrosion behavior of materials.

Inconel 718 alloy is a common superalloy that is created for turbine blades in planes. For the planes that are used in marine environments, turbine blades undergo marine corrosion, causing them to fail. However, the corrosion behavior and passivation properties of Inconel 718 alloys are rarely reported in marine environments. This work aims to contribute to a better understanding of the passive film formed on an Inconel 718 alloy fabricated using SLM and to compare it with a commercially rolled Inconel 718 alloy.

2. Experimental Details

The materials used in the present work were an Inconel 718 alloy fabricated using selective laser melting (SLM 718) and a commercially rolled Inconel 718 alloy (R 718, which was used as a reference material). SLM 718 was manufactured at a power of 138 W, a scanning rate of 429 mm/s, and a material plate thickness of 0.04 mm. The chemical compositions (wt.%) of SLM 718 and R 718 are shown in Table 1. The samples were cut into cylinders with a diameter of 10 mm and sealed in a mixture of epoxy and polyamide resins with 0.785 cm^2 of the surface exposed. Then, samples were gradually ground with SiC papers up to 1000 grit, cleaned in ethanol, and finally dried in cold air.

The electrochemical tests were performed in a 3.5 wt.% NaCl solution at 25 ± 1 °C. The horizontal plane of the SLM 718 alloy was selected as the research plane. The potentiodynamic polarization measurement was performed at a scan rate of 0.1667 mV/s from -250 mV_{SCE} below the open-circuit potential (OCP) to 1100 mV_{SCE}. Electrochemical impedance spectroscopy (EIS) measurements were conducted under natural corrosion conditions. The frequency ranged from 10^4 Hz to 10^{-2} Hz, and the AC amplitude was 10 mV. Potentiostatic polarization tests were carried out at 0.4 V_{SCE} for 1 h. Mott-Schottky tests were performed at an alternating current (AC) amplitude of 10 mV within an applied potential range of -600 mV_{SCE} to 1200 mV_{SCE} at a successive step of 20 mV after the potentiostatic polarization test. The electrochemical measurement methods used in the present work were described in detail in a previous study (Ref 25).

The phase constituents of the alloys were analyzed using X-ray diffraction (XRD, D/Max 2400 Rigaku Corporation, Tokyo, Japan) with a Cu Kα radiation source at 10 kV and 35 mA along with a step size of 0.02° and a scan rate of 4°/min. OM (optical microscopy) images were obtained using a Keyence VHX-700 (Keyence Co. Ltd., Osaka, Japan). The samples subjected to X-ray photoelectron spectroscopy (XPS) analysis were potentiostatically polarized at 400 mV_{SCE} for 1 h. XPS spectra were collected using an X-ray photoelectron spectrometer (ESCALAB 250Xi T) with an Al Kα (1486.6 eV) monochromatic radiation source. All the high-resolution spectra were fitted by Avantage software, and then the oxide data were obtained. After the immersion of freshly polished samples in a 3.5 wt.% NaCl solution for 24 h, the morphology of the corroded surface was studied using atomic force microscopy (AFM, ICSPI. Corp, Canada) in noncontact mode.

Table 1 Chemical compositions of SLM 718 and R 718 (wt.%)

	Ni	Cr	Nb	Mo	Ti	Al	Co	Cu	Mn	Fe
SLM 718	52.53	19.00	5.10	3.02	0.96	0.48	0.031	0.035	0.074	Bal.
R 718	53.20	19.20	5.10	3.10	0.90	0.30	0.85	0.25	0.29	Bal.

3. Results and Discussion

3.1 Microstructural Characterization

The XRD patterns of SLM 718 and R 718 are shown in Fig. 1. The diffraction peaks presented in Fig. 1 corresponded to the characteristics of γ-face centered cubic Ni-Fe-Cr, γ′-face centered cubic $Ni_3(Al,Ti)C$ (Ref 26) and γ″-body-centered cubic Ni_3Nb phases (Ref 27, 28). The (OM) images of SLM 718 and R 718 are shown in Fig. 2. Regarding SLM 718, various deposition traces were found, which clearly showed the laser scanning line by line in the horizontal direction and the molten pool with arc-shaped features formed layer by layer in the vertical direction, as shown in Fig. 2(a). R 718 has an equiaxed grain structure (Ref 29), with an average grain size of approximately 20 μm, as shown in Fig. 2(b). The chemical compositions of SLM 718 and R 718 were very similar, but their microstructures differed significantly.

3.2 Electrochemical Response

3.2.1 Open-Circuit Potential. Figure 3 shows the open-circuit potential (OCP) curves of SLM 718 and R 718 in a 3.5 wt.% NaCl solution. Figure 3 shows that the OCP of both alloys continuously shifted in the positive direction with an increasing immersion time and achieved its steady-state potential when the immersion time was 3000 s. This finding suggested that the passive film formed spontaneously on the surface of the two tested alloys (Ref 30). The steady-state potentials of SLM 718 and R 718 were -0.19 V_{SCE} and -0.13 V_{SCE}, respectively.

3.2.2 Potentiodynamic Polarization. Figure 4 presents the potentiodynamic polarization curves of SLM 718 and R 718 in a 3.5 wt.% NaCl solution. As seen from Fig. 4, both alloys exhibited typical active-passive behavior. The corrosion behaviors of SLM 718 and R 718 were similar but their E_{corr} and i_p were notably different. The corrosion potential (E_{corr}), corrosion current density (i_{corr}), and passive current density (i_p) derived from Fig. 4 are listed in Table 2. SLM 718 exhibited a relatively high passive current density, suggesting a faster dissolution rate. The increase in i_p and dissolution rate was related to the decrease in the Cr and Ni content in the passive film, which is illustrated later in this article (Ref 31). It is well known that the corrosion resistance of metals/alloys is closely

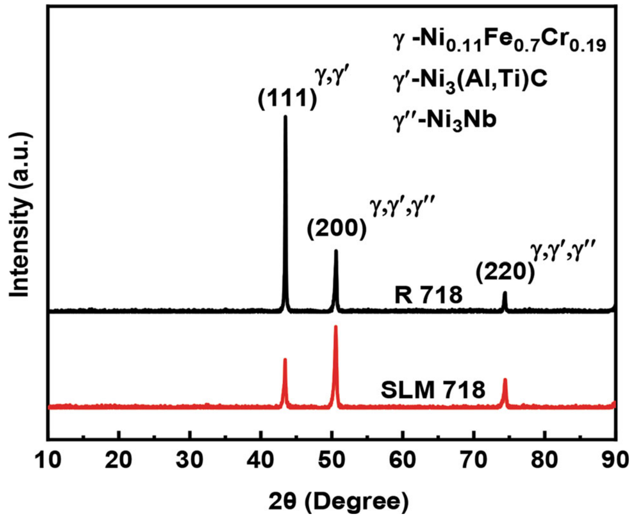

Fig. 1 XRD patterns of SLM 718 and R 718

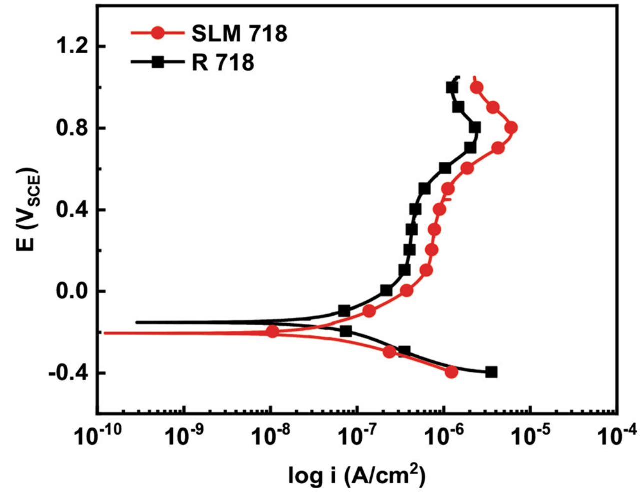

Fig. 4 Potentiodynamic polarization curves of the SLM 718 alloy and R 718 alloy

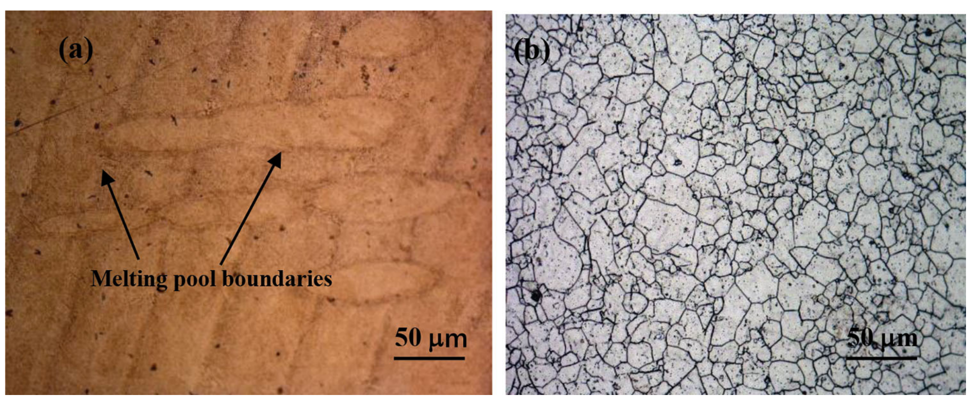

Fig. 2 OM images of the SLM 718 alloy (a) and R 718 alloy (b)

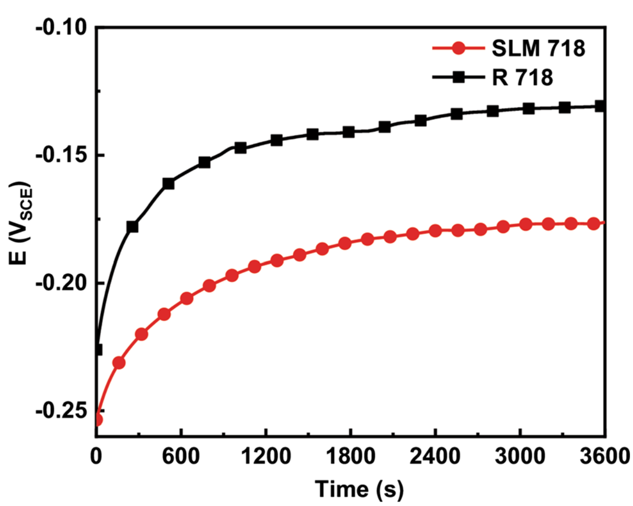

Fig. 3 OCP evolution of the SLM 718 alloy and R 718 alloy over time

Table 2. Electrochemical parameters extracted from the potentiodynamic polarization curves

	E_{corr}, mV$_{SCE}$	i_{corr}, A·cm^{-2}	i_p, A·cm^{-2}
SLM 718	−200 ± 5.20	1.12 ± 0.04 × 10^{-7}	2.37 ± 0.03 × 10^{-6}
R 718	−150 ± 1.30	1.79 ± 0.22 × 10^{-8}	1.24 ± 0.02 × 10^{-6}

related to the properties of their passive films (Ref 32). Therefore, it is obvious that the corrosion resistance of SLM 718 was inferior to that of R 718.

3.2.3 Electrochemical Impedance Spectroscopy. The Nyquist and Bode plots of SLM 718 and R 718 in a 3.5 wt.% NaCl solution are shown in Fig. 5. The Nyquist plots showed an incomplete semicircle arc, which indicated highly capacitive behavior (Ref 30, 33). This capacitive behavior suggested that

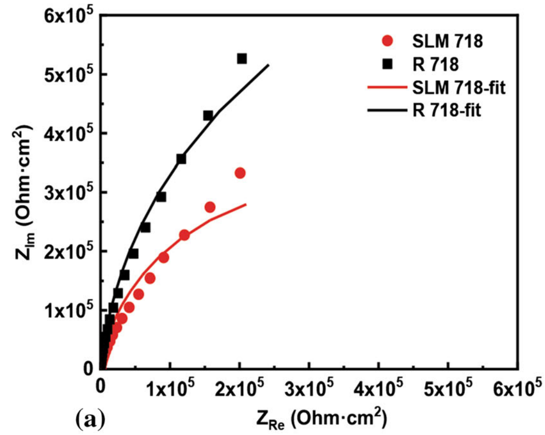

Fig. 5 Nyquist (a) and Bode (b) plots of the SLM 718 alloy and R 718 alloy.

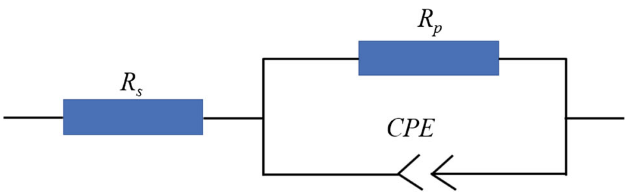

Fig. 6 Equivalent circuit used for the quantitative evaluation of electrochemical impedance spectroscopy

the corrosion mechanism of SLM 718 and R 718 was dominated by the passive film. The Bode plots showed that the phase angles tended toward −80° in the frequency range from approximately 10^{-1} to 10^{2} Hz, indicating the superior protectiveness of the passive film (Ref 34). The impedance of the passive film on SLM 718 was lower than that on R 718, indicating that SLM 718 had inferior corrosion resistance (Ref 35). The EIS only had one time constant (Ref 30, 36, 37), as shown in Fig. 5(b). The capacitance corresponding to the double layer was not observed. Figure 6 shows the eq

uivalent electric circuit of the EIS results. R_s is the solution resistance, R_p is the resistance of the passive film, and Q is the passive film capacitance that is expressed using the CPE. CPE was used due to the uneven current distribution at the surface or in the event of increased surface roughness. Table 3 lists the fitting results of the EIS data in Fig. 5. The R_p of R 718 was much higher than that of SLM 718, suggesting that the passive film of SLM 718 had inferior protective capacity (Ref 13). Therefore, the corrosion resistance of SLM 718 was inferior to that of R 718. This finding was in good agreement with the results obtained from the potentiodynamic polarization tests.

3.2.4 Potentiostatic Measurements. Figure 7 presents the potentiostatic polarization plots of SLM 718 and R 718 in a 3.5 wt.% NaCl solution. As seen in Fig. 7(a), the current densities decreased dramatically in the beginning due to the formation and thickening of the passive films (Ref 37). The current densities finally stabilized at $1.21 \pm 0.09 \times 10^{-7}$ and $1.04 \pm 0.08 \times 10^{-7}$ A/cm^2 for SLM 718 and R 718, respectively. A higher current density means that the formed passive film is more stable and vice versa. Thus, the passive film of SLM 718 was more easily corroded than that of R 718. The slopes (k) of the curves for SLM 718 and R 718 were −0.88 and −0.91, respectively. Briefly, $k = -1$ suggests that the passive film is compact and highly protective, whereas $k = -0.5$ indicates that the film is porous (Ref 12, 13, 38, 39). Compared with R 718, the k value of SLM 718 decreased significantly, which meant that the compactness of the passive film on SLM 718 decreased. A passive film with high compactness can effectively restrain the damage caused by corrosive substances, thus reducing the dissolution rate of the passive film. (Ref 40) Hence, the protective property of the passive film on SLM 718 was of inferior quality.

3.3 Mott–Schottky Analysis

It is well known that the semiconductor properties of passive films are closely related to their corrosion resistance. Mott–Schottky analysis was performed to investigate the semiconductor properties of the passive film. According to Mott–Schottky theory, the space-charge capacitance of a semiconductor is expressed as (Ref 41, 42)

$$\frac{1}{C_{SC}^2} = \frac{2}{\varepsilon\varepsilon_0 e N_D A^2}\left(V - V_{FB} - \frac{k_B T}{e}\right) \quad \text{for n - type} \qquad \text{(Eq 1)}$$

$$\frac{1}{C_{SC}^2} = \frac{2}{\varepsilon\varepsilon_0 e N_A A^2}\left(V - V_{FB} - \frac{k_B T}{e}\right) \quad \text{for p - type} \qquad \text{(Eq 2)}$$

runwhere ε is the dielectric constant of the passive film (12 for Cr_2O_3 (Ref 13, 43)), ε_0 is the vacuum permittivity constant (8.854×10^{-14} F/cm), e is the elementary charge (1.602×10^{-19} C), A is the electrode surface area, V is the applied potential, V_{FB} is the flat band potential, k_B is the Boltzmann constant (1.38×10^{-23} J/K), T is the absolute temperature, N_D is the donor density, and N_A is the donor density. Thus, a positive slope corresponds to n-type semiconductors, and a negative slope corresponds to p-type semiconductors.

Table 3 EIS fitted data of the SLM 718 alloy and R 718 alloy

	R_s, Ω·cm^{-2}	Q, Ω^{-1}s^{n}cm^{-2}	n	R_p, Ω·cm^{-2}
SLM 718	6.19 ± 0.08	3.02 ± 0.02×10^{-5}	0.93 ± 0.01	6.83 ± 0.26×10^{5}
R 718	6.08 ± 0.04	2.19 ± 0.01×10^{-5}	0.95 ± 0.01	1.63 ± 0.04×10^{6}

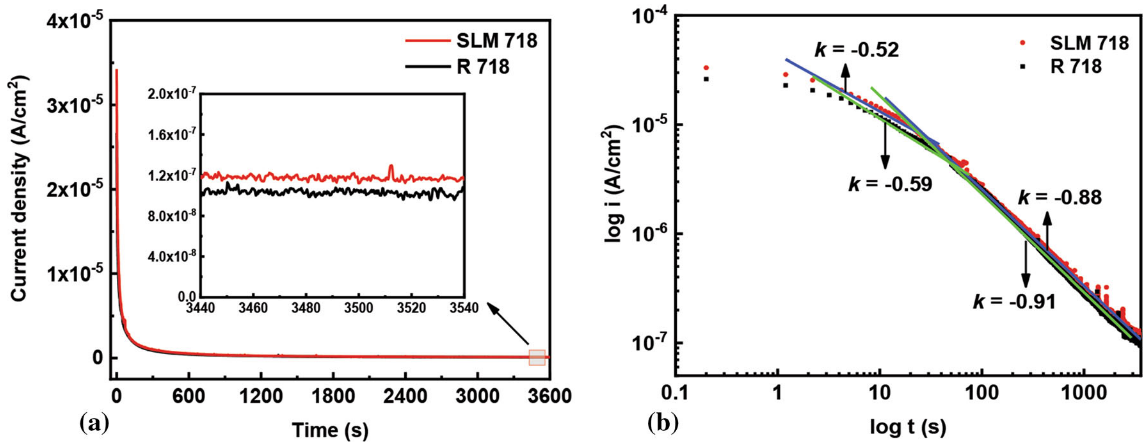

Fig. 7 *i-t* (a) and logi-logt (b) plots of the SLM 718 alloy and R 718 alloy in a 3.5 wt.% NaCl solution

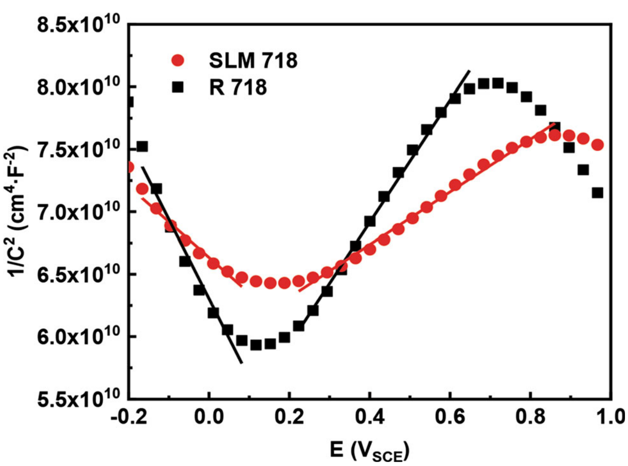

Fig. 8 Mott–Schottky plots of the SLM 718 alloy and R 718 alloy

Table 4 N_a **and** N_d **values of the passive films on SLM 718 and R 718**

	N_a, cm^{-3}	N_d, cm^{-3}
SLM 718	1.16 × 10^{21}	1.03 × 10^{21}
R 718	1.63 × 10^{20}	7.06 × 10^{20}

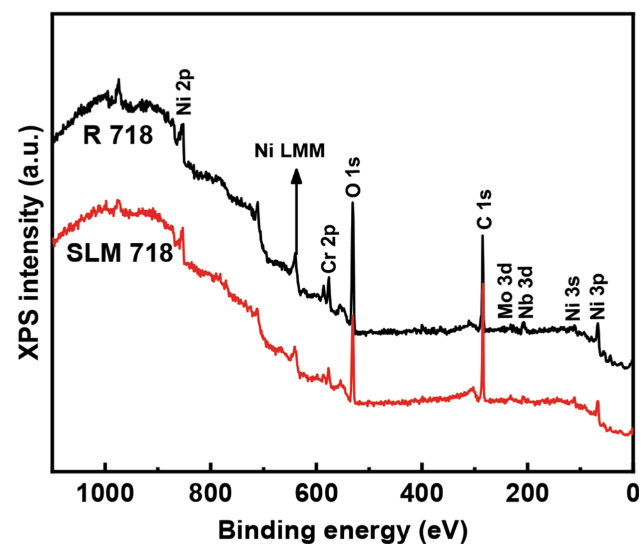

Fig. 9 XPS survey of the passive films formed on the SLM 718 alloy and R 718 alloy after potentiostatic polarization

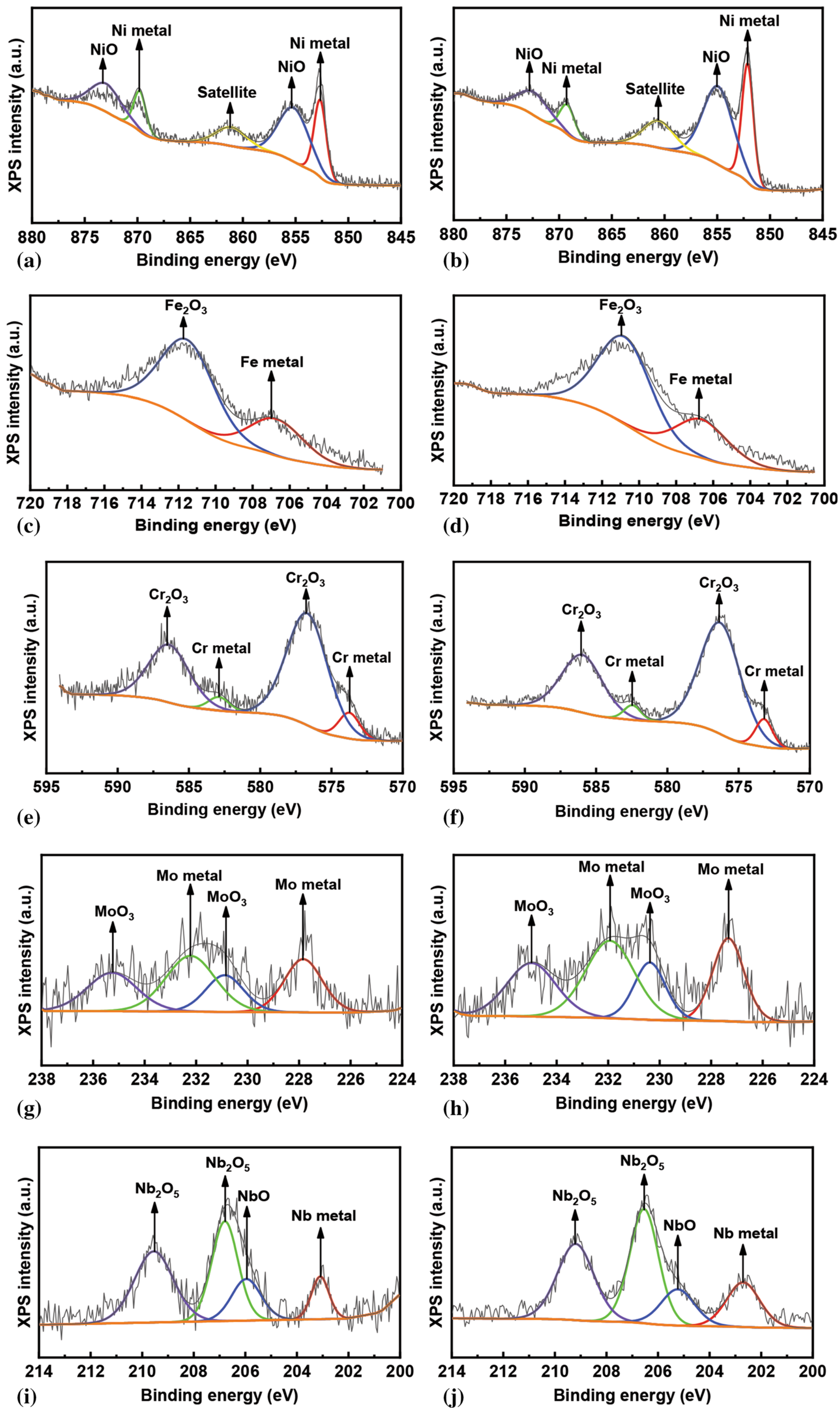

Fig. 10 High-resolution Ni 2p, Fe 2p, Cr 2p, Mo3d and Nb3d XPS spectra of the passive films formed on SLM 718 (a) (c) (e) (g) (i) and R 718 (b) (d) (f) (h) (j)

Table 5 Chemical composition (at.%) of the passive films formed on the SLM 718 alloy and R 718 alloy

	NiO	Fe_2O_3	Cr_2O_3	MoO_3	NbO	Nb_2O_5
SLM 718	39.34	14.57	37.87	3.52	0.87	3.84
R 718	20.89	17.35	51.72	3.52	1.05	5.47

The Mott–Schottky plots of the passive film on SLM 718 and R 718 are shown in Fig. 8, and the passive films of SLM 718 and R 718 show p-type and n-type semiconducting characteristics (Ref 44). The passive films acted as a p-type semiconductor below 0.1 V_{SCE} due to the presence of some compounds, such as Cr_2O_3 and NiO (Ref 45). However, they exhibited n-type semiconductor behavior above 0.1 V_{SCE} due to the presence of Fe_2O_3 (Ref 46). The acceptor and/or donor densities (N_a/N_d) calculated from Fig. 10 are listed in Table 4. SLM 718 had higher values of N_a and N_d than R 718. In addition, when the metals were covered with a passive film layer, N_a/N_d was the key factor dominating the corrosion current density of the passive film (Ref 38). Therefore, the larger passive current density of SLM 718 could be attributed to the higher N_a or N_d (Ref 47, 48). The Mott–Schottky analysis suggested that the passive film on SLM 718 was defective. This finding was in good agreement with previous work showing that passive films of additively manufactured alloys were usually defective (Ref 17). The results of the Mott–Schottky analysis were consistent with the results of the polarization curves and EIS test.

3.4 XPS Analysis of the Passive Film

Figure 9 shows the XPS spectra of the passive films formed on SLM 718 and R 718, and the passive films contain C 1s, O 1s, Ni 2p, Fe 2p, Cr 2p, Mo 3d, and Nb 3d peaks; the C came from contamination when the samples were exposed to air. No significant differences were found in the chemical composition of the passive films formed on SLM 718 and R 718. Figure 10 shows the high-resolution Ni 2p, Fe 2p, Cr 2p, Mo 3d, and Nb 3d XPS spectra of the passive films formed on the SLM 718 and R 718 alloys. The Ni 2p XPS spectrum could be divided into Ni^{2+} (NiO) and metallic Ni. The existence of satellite peaks is a well-known feature associated with certain elements (such as Ni) (Ref 49). The Fe 2p XPS spectrum could be divided into Fe^{3+} (Fe_2O_3) and metallic Fe. The Cr 2p XPS spectrum could be divided into Cr^{3+} (Cr_2O_3) and metallic Cr (Ref 50). The Mo 3d XPS spectrum could be divided into Mo^{6+} (MoO_3) and metallic Mo. The Nb 3d XPS spectrum could be divided into Nb^{5+} (Nb_2O_5), Nb^{2+} (NbO), and metallic Nb. The passive films on SLM 718 and R 718 were composed of Cr_2O_3, Fe_2O_3, NiO, MoO_3, Nb_2O_5 and NbO. As seen in Table 5, Cr_2O_3, NiO, and Fe_2O_3 were the dominant components in the passive film. This finding was consistent with published XPS results on Ni-Cr-Fe alloys, in which their passive films consisted of Cr_2O_3 and NiO (Ref 51). In comparison with R 718, the passive film formed on SLM 718 contained more NiO, which was porous and less protective than Cr_2O_3. A high Cr_2O_3 percentage in a passive film is an indication of a compact surface oxide. The Cr_2O_3 film had a lower point defect density and higher thermodynamic stability than the NiO layer (Ref 12), which led to an increase in the passive current density and dissolution rate of SLM 718. Therefore, the corrosion resistance of SLM 718 was inferior to that of R 718.

3.5 AFM

The surface corrosion morphology was further examined using AFM, and the 3D morphology of the surface corrosion of SLM 718 and R 718 is shown in Fig. 11. As seen in Fig. 11, the surface roughness of SLM 718 (20.02 ± 0.12 nm) was slightly larger than that of R 718 (19.79 ± 0.11 nm). The presence of an undulating pattern in Fig. 11(a), which revealed that uneven corrosion was present in SLM 718, was attributed to the layered structure of the formed melting traces (Fig. 2a). The surface profile of R 718 suggested uniform corrosion.

4. Conclusion

In this study, the corrosion behavior and passive films of SLM 718 and R 718 alloys were investigated. The main conclusions can be summarized as follows:

(1) Both the SLM 718 and R 718 alloys were composed of γ, γ' and γ'' phases. SLM 718 had obvious molten pool boundaries, while R 718 had equiaxed grains.
(2) In the electrochemical test, SLM 718 exhibited lower corrosion resistance than the rolled alloy in a 3.5 wt.% NaCl solution at room temperature.
(3) The passive films of the SLM 718 and R 718 alloys were composed of Cr_2O_3, Fe_2O_3, NiO, MoO_3, Nb_2O_5 and NbO, and the porous passive film formed on SLM 718 had less Cr_2O_3 and more NiO, thereby exhibiting inferior corrosion resistance compared with the film formed on the rolled alloy.

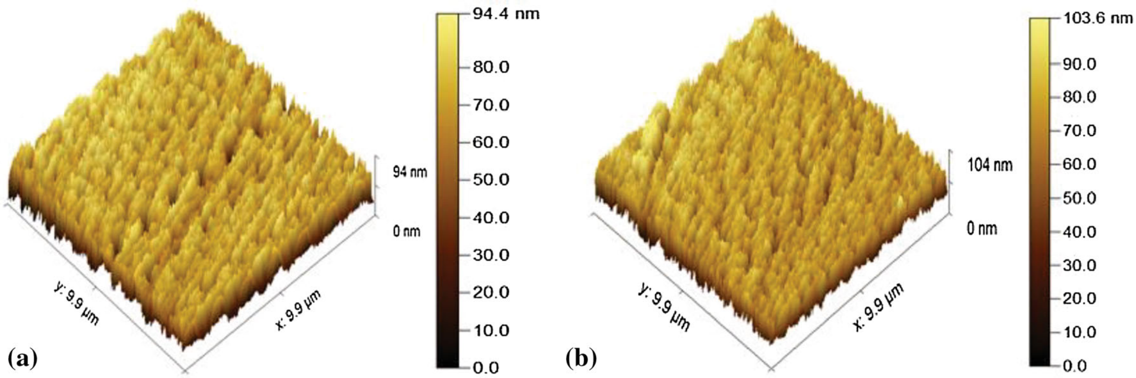

Fig. 11 AFM micrographs of SLM 718 (a) and R 718 (b)

Acknowledgment

This work was financially supported by National Key Research and Development Program of China (No. 2018YFC0309100), National Natural Science Foundation of China (Nos. 52001142 and 51401092) and the Natural Science Foundation of the Jiangsu Higher Education Institutions of China (No. 19KJB580010).

Reference

1. L.Y. Wang, H.P. Li, Q.Y. Liu, L.P. Xu, S. Lin and K. Zheng, Effect of Sodium Chloride on the Electrochemical Corrosion of Inconel 625 at High Temperature and Pressure, *J. Alloys Compd.*, 2017, **703**, p 523–529
2. L.D. Teng, T.T. Zhao, T.F. Cheng and Y.T. Yang, Microstructure Evolution and Corrosion Behavior of Nb-Alloyed Cast Heat-Resistant Steel During Different Aging Treatments, *J. Iron Steel Res. Int.*, 2020, **27**, p 1456–1465
3. L.L. Yang, J.L. Wang, R.Z. Yang, S.S. Yang, Y.X. Jia, M.H. Chen, Y.X. Qiao, P.Y. Guo, S.L. Zhu and F.H. Wang, Oxidation Behavior of a Nanocrystalline Coating with Low Ta Content at High Temperature, *Corros. Sci.*, 2021, **180**, p 109182
4. B.C. Zhang, M.Z. Xiu, Y.T. Tan, J. Wei and P. Wang, Pitting Corrosion of SLM Inconel 718 Sample Under Surface and Heat Treatments, *Appl. Surf. Sci.*, 2019, **490**, p 556–567
5. E.O. Ezugwu, Z.M. Wang and A.R. Machado, The Machinability of Nickel-Based Alloys: A Review, *J. Mater. Process. Tech.*, 1999, **86**, p 1–16
6. S.X. Jin, H.L. Ma, E.Y. Lu, L. Zhou, Q.L. Zhang, P. Fan, Q.Z. Yan, D.Q. Yuan, X.Z. Cao and B.Y. Wang, Depth Distributions of Cavities in Advanced Ferritic/Martensitic and Austenitic Steels with High Helium Preimplantation and High Damage Level, *Mater. Today Energy*, 2021, **20**, p 100687
7. T. Kurzynowski, I. Smolina, K. Kobiela, B. Kuźnicka and E. Chlebus, Wear and Corrosion Behaviour of Inconel 718 Laser Surface Alloyed with Rhenium, *Mater. Des.*, 2017, **132**, p 349–359
8. M.E. Aydinöz, F. Brenne, M. Schaper, C. Schaak, W. Tillmann, J. Nellesen and T. Niendorf, On the Microstructural and Mechanical Properties of Post-Treated Additively Manufactured Inconel 718 Superalloy Under Quasi-Static and Cyclic Loading, *Mater. Sci. Eng. A*, 2016, **669**, p 246–258
9. R. Firoz, S.K. Basantia, N. Khutia, H.N. Bar, S. Sivaprasad and G.V.S. Murthy, Effect of Microstructural Constituents on Mechanical Properties and Fracture Toughness of Inconel 718 with Anomalous Deformation Behavior at 650 °C, *J. Alloys Compd.*, 2020, **845**, p 156276
10. S. Gorsse, C. Hutchinson, M. Goune and R. Banerjee, Additive Manufacturing of Metals: A Brief Review of the Characteristic Microstructures and Properties Of Steels, Ti-6Al-4V and High-Entropy Alloys, *Sci. Technol. Adv. Mater.*, 2017, **18**, p 584–610
11. J.J. Yang, H.H. Yang, H.C. Yu, Z.M. Wang and X.Y. Zeng, Corrosion Behavior of Additive Manufactured Ti-6Al-4V Alloy in NaCl Solution, *Metall. Mater. Trans. A*, 2017, **48**, p 3583–3593
12. L.N. Zhang and O.A. Ojo, Corrosion Behavior of Wire Arc Additive Manufactured Inconel 718 Superalloy, *J. Alloys Compd.*, 2020, **829**, p 154455
13. L. Liu, Y. Li and F.H. Wang, Influence of Micro-Structure on Corrosion Behavior of a Ni-Based Superalloy in 35% NaCl, *Electrochim. Acta*, 2007, **52**, p 7193–7202
14. W.P. Zhang, L.G. Song, T. Zhu, Y. Xiong, H.L. Ma, Q.Z. Yan, X.Z. Cao, B.Y. Wang and S.X. Jin, Investigation of Spatial Relationship Between Helium Bubbles and Dislocation Loops in RAFM Steel, *J. Nucl. Mater.*, 2021, **548**, p 152862
15. P.R. Zhang and Z.Q. Liu, Physical-Mechanical and Electrochemical Corrosion Behaviors of Additively Manufactured Cr-Ni-Based Stainless Steel Formed by Laser Cladding, *Mater. Des.*, 2016, **100**, p 254–262
16. D.C. Kong, C.F. Dong, X.Q. Ni, L. Zhang, H. Luo, R.X. Li, L. Wang, C. Man and X.G. Li, The Passivity of Selective Laser Melted 316L Stainless Steel, *Appl. Surf. Sci.*, 2020, **504**, p 144495
17. C. Örnek, Additive Manufacturing—A General Corrosion Perspective, *Corros. Eng. Sci. Technol.*, 2018, **53**, p 531–535
18. B.T. Wu, Z.X. Pan, S.Y. Li, D. Cuiuri, D.H. Ding and H.J. Li, The Anisotropic Corrosion Behaviour of Wire Arc Additive Manufactured Ti-6Al-4V Alloy in 35% NaCl Solution, *Corros. Sci.*, 2018, **137**, p 176–183
19. X.Q. Ni, D.C. Kong, Y. Wen, L. Zhang, W.H. Wu, B.B. He, L. Lu and D.X. Zhu, Anisotropy in Mechanical Properties and Corrosion Resistance of 316L Stainless Steel Fabricated by Selective Laser Melting, *Int. J. Min. Metall. Mater.*, 2019, **26**, p 319–328
20. D.C. Kong, X.Q. Ni, C.F. Dong, L. Zhang, J.Z. Yao, C. Man, L. Wang, K. Xiao and X.G. Li, Anisotropic Response in Mechanical and Corrosion Properties of Hastelloy X Fabricated by Selective Laser Melting, *Const. Build. Mater.*, 2019, **221**, p 720–729
21. C. Juillet, A. Oudriss, J. Balmain, X. Feaugas and F. Pedraza, Characterization and Oxidation Resistance Of Additive Manufactured and Forged IN718 Ni-Based Superalloys, *Corros. Sci.*, 2018, **142**, p 266–276
22. T.M. Chiu, M. Mahmoudi, W. Dai, A. Elwany, H. Liang and H. Castaneda, Corrosion Assessment of Ti-6Al-4V Fabricated Using Laser Powder-Bed Fusion Additive Manufacturing, *Electrochim. Acta*, 2018, **279**, p 143–151
23. D.C. Kong, C.F. Dong, X.Q. Ni and X.G. Li, Corrosion of Metallic Materials Fabricated by Selective Laser Melting, *npj Mater. Degrad.*, 2019, **3**, p 24
24. D.C. Kong, C.F. Dong, S.L. Wei, X.Q. Ni, L. Zhang, R.X. Li, L. Wang, C. Man and X.G. Li, About Metastable Cellular Structure in Additively Manufactured Austenitic Stainless Steels, *Addit. Manuf.*, 2021, **38**, p 101804
25. Y.X. Qiao, S.L. Sheng, L.M. Zhang, J. Chen, L.L. Yang, H.L. Zhou, Y.X. Wang, H.B. Li and Z.B. Zheng, Friction and Wear Behaviors of a High Nitrogen Austenitic Stainless Steel Fe-19Cr-15Mn-066N, *J Min Metall Sect B-Metall*, 2021 https://doi.org/10.2298/JMMB201026025Q
26. G.H. Cao, T.Y. Sun, C.H. Wang, X. Li, M. Liu, Z.X. Zhang, P.F. Hu, A.M. Russell, R. Schneider, D. Gerthsen, Z.J. Zhou, C.P. Li and G.F. Chen, Investigations of γ', γ'' and δ Precipitates in Heat-Treated Inconel 718 Alloy Fabricated by Selective Laser Melting, *Mater. Charact.*, 2018, **136**, p 398–406

27. B. Anush Raj, J.T. Winowlin Jappes, M. Adam Khan, V. Dillibabu and N.C. Brintha, Direct Metal Laser Sintered (DMLS) Process to Develop Inconel 718 Alloy for Turbine Engine Components, *Optik*, 2020, **202**, p 163735
28. M. Sundararaman, P. Mukhopadhyay and S. Banerjee, Some Aspects of the Precipitation of Metastable Intermetallic Phases in INCONEL 718, *Metall. Mater. Trans. A*, 1992, **23**, p 2015–2028
29. Z.R. Ye, Z.C. Qiu, Z.B. Wang, Y.G. Zheng, R. Yi and X. Zhou, Can the Prior Cathodic Polarisation Treatment Remove the Air-Formed Surface Film and is it Necessary for the Potentiodynamic Polarisation Test?, *Acta Metall. Sin.*, 2020, **33**, p 839–845
30. Z.G. Liu, X.H. Gao, M. Xiong, P. Li, R.D.K. Misra, D.Y. Rao and Y.C. Wang, Role of Hot Rolling Procedure and Solution Treatment Process on Microstructure, Strength and Cryogenic Toughness of High Manganese Austenitic Steel, *Mater. Sci. Eng. A*, 2021, **807**, p 140881
31. L.O. Osoba, A.M. Oladoye and V.E. Ogbonna, Corrosion Evaluation of Superalloys Haynes 282 and Inconel 718 in Hydrochloric Acid, *J. Alloys Compd.*, 2019, **804**, p 376–384
32. D.P. Wang, H.T. Zhang, P.Y. Guo, B.A. Sun and Y.X. Wang, Nanoscale Periodic Distribution of Energy Dissipation at the Shear Band Plane in a Zr-Based Metallic Glass, *Scripta Mater.*, 2021, **197**, p 113784
33. Y.X. Qiao, D.K. Xu, S. Wang, Y.J. Ma, J. Chen, Y.X. Wang and H.L. Zhou, Effect of Hydrogen Charging on Microstructural Evolution and Corrosion Behavior of Ti-4Al-2V-1Mo-1Fe Alloy, *J. Mater. Sci. Technol.*, 2021, **60**, p 168–176
34. E.E. Oguzie, J.B. Li, Y.Q. Liu, D.M. Chen, Y. Li, K. Yang and F.H. Wang, The Effect of Cu addition on the Electrochemical Corrosion and Passivation Behavior of Stainless Steels, *Electrochim. Acta*, 2010, **55**, p 5028–5035
35. H. Nady, M.M. El-Rabiei and M. Samy, Corrosion Behavior and Electrochemical Properties of Carbon Steel, Commercial Pure Titanium, Copper and Copper-Aluminum-Nickel Alloy in 35% Sodium Chloride Containing Sulfide Ions, *Egypt. J. Petrol.*, 2017, **26**, p 79–94
36. Y. Li and Y.F. Cheng, Passive Film Growth on Carbon Steel and its Nanoscale Features at Various Passivating Potentials, *Appl. Surf. Sci.*, 2017, **396**, p 144–153
37. Z. Wang, Z.Q. Zhou, L. Zhang, J.Y. Hu, Z.R. Zhang and M.X. Lu, Effect of pH on the Electrochemical Behaviour and Passive Film Composition of 316l Stainless Steel, *Acta Metall Sin*, 2018, **32**, p 585–598
38. L. Liu, Y. Li and F.H. Wang, Influence of Nanocrystallization on Passive Behavior of Ni-Based Superalloy in Acidic Solutions, *Electrochim. Acta*, 2007, **52**, p 2392–2400
39. Y.X. Qiao, J. Huang, D. Huang, J. Chen, W. Liu, Z.B. Wang and Z.B. Zheng, Effects of Laser Scanning Speed on Microstructure, Microhardness and Corrosion Behavior of Laser Cladding Ni45 Coatings, *J. Chem.*, 2020, **2020**, p 1438473
40. H.Q. Fan, W.C. Xu, L. Wei, Z.H. Zhang, Y.B. Liu and Q. Li, Relationship Between La and Ce Additions on Microstructure and Corrosion Resistance of Hot-Dip Galvanized Steel, *J. Iron Steel Res. Int.*, 2020, **27**, p 1108–1116
41. D.C. Kong, A.N. Xu, C.F. Dong, F.X. Mao, K. Xiao, X.G. Li and D.D. Macdonald, Electrochemical Investigation and ab Initio Computation Of Passive Film Properties on Copper in Anaerobic Sulphide Solutions, *Corros Sci*, 2018, **116**, p 34–43
42. Z.X. Li, L.M. Zhang, A.L. Ma, J.X. Hu, S. Zhang, E.F. Daniel and Y.G. Zheng, Comparative Study on the Cavitation Erosion Behavior of Two Different Rolling Surfaces on 304 Stainless Steel, *Tribol. Int.*, 2021, **159**, p 106994
43. L.M. Zhang, Z.X. Li, J.X. Hu, A.L. Ma, S. Zhang, E.F. Daniel, A.J. Umoh, H.X. Hu and Y.G. Zheng, Understanding the Roles of Deformation-Induced Martensite of 304 Stainless Steel in Different Stages of Cavitation Erosion, *Tribol. Int.*, 2021, **155**, p 106752
44. Z.C. Feng, X.Q. Cheng, C.F. Dong, L. Xu and X.G. Li, Passivity of 316L Stainless Steel in Borate Buffer Solution Studied by Mott-Schottky Analysis, Atomic Absorption Spectrometry and X-ray Photoelectron Spectroscopy, *Corros. Sci.*, 2010, **52**, p 3646–3653
45. S. Maximovitch, Influence of Formation Conditions on Impedance Properties of Nickel Passive Layers Formed in 1 M KOH, *Electrochim. Acta*, 1996, **41**, p 2761–2771
46. S.P. Carmelo Sunseri and F. Di Quarto, Photocurrent spectroscopic investigations of passive films on chromium, *J. Electrochem. Soc.*, 1990, **137**, p 2411–2417
47. S.J. Ahn and H.S. Kwon, Effects of Solution Temperature on Electronic Properties of Passive Film Formed on Fe in pH 8.5 Borate Buffer Solution, *Electrochim. Acta*, 2004, **49**, p 3347–3353
48. Y.X. Qiao, Y.P. Chen, L.L. Li, J. Chen, X.J. Wang, L.L. Yang, H.L. Zhou, Z.B. Wang and Z.H. Guo, Corrosion Behavior of a Nickel-Free High-Nitrogen Stainless Steel With Hydrogen Charging, *JOM*, 2021, **73**, p 1165–1172
49. M.S. Bakare, K.T. Voisey, M.J. Roe and D.G. McCartney, X-ray Photoelectron Spectroscopy Study of the Passive Films Formed on Thermally Sprayed and Wrought Inconel 625, *Appl. Surf. Sci.*, 2010, **257**, p 786–794
50. S. Hong, J.R. Lin, Y.P. Wu, J.H. Wu, Y. Zheng, Y.Q. Zhang, J.B. Cheng and W. Sun, Cavitation Erosion Characteristics at Various Flow Velocities in NaCl Medium of Carbide-Based Cermet Coatings Prepared by HVOF Spraying, *Ceram. Int.*, 2021, **47**, p 1929–1939
51. P. Jakupi, D. Zagidulin, J.J. Noël and D.W. Shoesmith, The Impedance Properties of the Oxide Film on the Ni-Cr-Mo Alloy-22 in Neutral Concentrated Sodium Chloride Solution, *Electrochim. Acta*, 2011, **56**, p 6251–6259